International Journal of Microwave and Wireless Technologies, 2011, 3(3), 373–381.
doi:10.1017/S1759078711000225

RESEARCH PAPER

Multi-wavelength radar target detection in an extreme advection duct event

ROBERT E. MARSHALL AND KATHERINE L. HORGAN

Near sea surface radio frequency (RF) refraction is four dimensional (4D) and can significantly impact the performance of radar systems. The refractivity field is dictated by the vertical thermodynamic structure of the constantly evolving marine atmospheric boundary layer (MABL). Logistical and budgetary restraints on meteorological measurements over water to capture the spatio-temporal structure of refractivity fields influencing radar performance have limited the knowledge of how and why radar performance is azimuth, range, and time dependent. Rapidly increasing computer processing speeds and decreasing memory capacity costs have supported the horizontal and vertical resolution requirements for mesoscale numerical weather prediction (NWP) models to resolve the thermodynamic structure in the MABL. Once modeled, refractivity structure is easily calculated from the thermodynamic structure. Mesoscale NWP models coupled with modern parabolic equation radar performance models can support the prediction of 4D radar performance in challenging non-homogeneous, near surface refractivity fields at the time and location of the modeler's choice. The NWP modeling presented in this paper demonstrates how large-scale offshore flow of warm and dry air over colder seas produces strong near surface RF trapping. Large land-sea temperature differences can produce near shore sea breezes and surface-based ducts. This paper describes modeled radar performance in such a complex ducting structure over the Persian Gulf during large-scale northwest atmospheric flow. The refractivity field was resolved by the Coupled Ocean/ Atmosphere Mesoscale Prediction System (COAMPS® is a registered trademark of the Naval Research Laboratory) and the notional radar performance was modeled by the advanced refractive effects prediction system (AREPS). The results indicate strong spatial and wavelength-dependent enhancements and degradations in radar performance relative to a standard atmosphere.

Keywords: refraction, radio frequency propagation

Received 15 October 2010; Revised 13 January 2011; first published online 4 April 2011

I. INTRODUCTION

Non-standard radio frequency (RF) propagation extends for hundreds of kilometers over the water when surface ducts are formed in stable internal boundary layers (SIBLs) due to offshore flow of warm and dry air over colder sea surfaces [1]. Surface ducts are created when the vertical gradient of modified refractivity (dM/dz) is less than zero. The vertical gradient of M is dependent on the vertical gradient of potential temperature ($d\theta/dz$) and the vertical gradient of water vapor mixing ratio (dw/dz) as shown in equation (1). Depending on temperature and relative humidity, the w gradient term can be two to six times the θ gradient term [2]:

$$\frac{dM}{dz} \approx 0.128 - c_1 \frac{d\theta}{dz} + c_2 \frac{dw}{dz}. \quad (1)$$

Table 1 lists the categories of refraction and the range of dM/dz that defines each category.

Naval Surface Warfare Center, 18444 Dahlgren Road, Suite 330, Dahlgren, Virginia, USA. Phone: 5406534751
Corresponding author:
R. E. Marshall
Email: erobert.e.marshall@navy.mil

For the standard and the normal range of propagation, RF energy gently refracts away from earth curvature. Within 100 km of the shoreline or near large-scale frontal boundaries, standard propagation is short lived. During ducting or trapping conditions, RF energy is bent downwards toward the sea surface where it is reflected back toward the top of the shallow duct and refracted again toward the surface. This type of pattern can be repeated for hundreds of kilometers downrange. Ducting creates radar holes and folded land and sea clutter. Super-refraction forces RF energy to hug earth curvature and extends radar horizon for hundreds of kilometers. Super refraction invites interference from distant emitters. Although a rarer meteorological event, sub-refraction rapidly curves RF energy away from earth curvature and is extremely expensive to ameliorate [3].

For the case study in this paper, warmer air flows offshore over colder water and a shallow stable internal boundary layer (SIBL) forms from the sea surface up to typically 50 m above sea level (ASL). These layers are characterized by a positive gradient in θ that nudges the left side of (1) toward zero. If the water vapor content in the air flowing from the land is less than that over the water surface, the vertical gradient of w in the SIBL will be negative usually to the degree of nudging the vertical gradient of M well below zero and creating a ducting environment. Mechanical turbulence tends to

Table 1. Propagation categories quantified by the vertical gradient of modified refractivity.

Behavior (dM/dz) m^{-1}	Range 1	Range 2
Standard		=0.118
Ducting	<0.0	
Super refractive	0.0	0.079
Normal	0.079	0.157
Sub-refractive		>0.157

vertically mix the water vapor and potential temperature gradients supporting these advection ducts in the downwind direction. SIBL or surface duct height is approximately proportional to the square root of the offshore distance, proportional to wind speed, and inversely proportional to the square root of the land-sea temperature difference. SIBL height is only slightly decreased for cases of higher water vapor content. The offshore distance to the location where the SIBL or surface duct is mixed to the point of normal propagation is proportional to wind speed and proportional to the square of the land-sea temperature difference [1]. For rather common combinations of wind speed and land-sea temperature differences, these surface ducts can exist for hundreds of kilometers offshore.

II. MODELS

Mesoscale numerical weather prediction (NWP) models have been employed to resolve refractivity fields since 1995 [4]. For the past 4 years, the Naval Surface Warfare Center, Dahlgren Division (NSWCDD) has exploited the technology for providing a 48 h radar performance forecast capability. This has been accomplished by combining a modern parabolic equation RF performance tool with a mesoscale NWP model. This combination allows for a globally locatable 48 h RF system forecast.

A) Radar system model

The advanced refractive effects prediction system (AREPS) was employed to model the performance of three notional radars at S-, C-, and X-band [5]. The notional radars are designed to have equal probability of detecting a notional target in free space allowing model output to be viewed in terms of wavelength influences due to refractivity fields. The radars are located 23 m ASL. AREPS is capable of accepting three dimensional (3D) refractivity fields generated by a mesoscale NWP model.

B) Refractivity field model

The 3D refractivity fields are provided by the Coupled Ocean/Atmosphere Mesoscale Prediction System (COAMPS®) [6]. COAMPS® is the US Navy operational mesoscale NWP model. COAMPS® provides a 0–48 h refractivity forecast. The COAMPS®/AREPS combination is run in a highly spatially resolved mode at NSWCDD in order to forecast radar and communication system performance at any location on the globe.

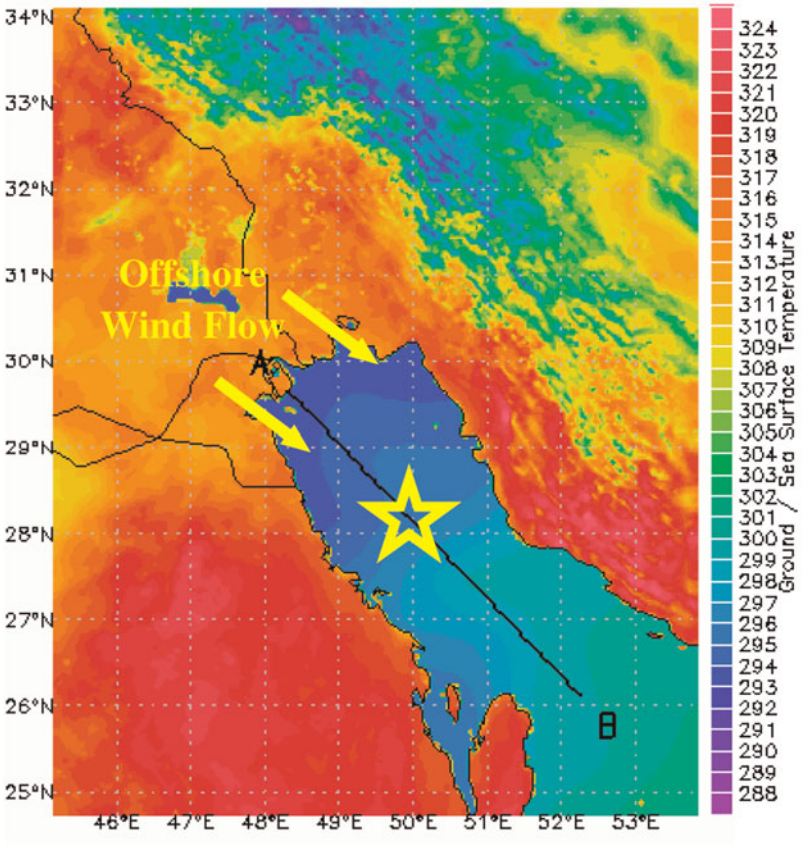

Fig. 1. Surface temperatures (K) as resolved by COAMPS® around and over the Persian Gulf at 1100 UTC on May 14, 2009. Notional radars are modeled at the star and located 210 km downwind from point A.

https://doi.org/10.1017/S1759078711000225 Published online by Cambridge University Press

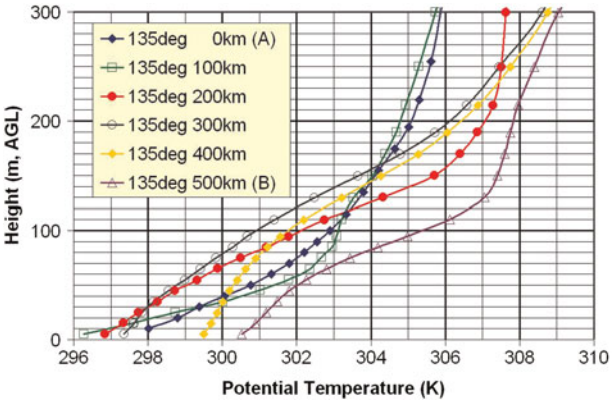

Fig. 2. Potential temperature every 100 km from A to B as modeled by COAMPS® for 1100 UTC on May 14, 2009. The positive slope indicates thermal stability due to warm air flowing over a colder sea.

III. CASE STUDY

On 14 May 2009, COAMPS® resolved the SIBL structure in northwest flow over the Persian Gulf. At 1100 UTC, the notional radars were modeled with AREPS and located in the COAMPS® refractivity field approximately 210km downwind in the middle of the Persian Gulf as shown by the star in Fig. 1. Figure 1 represents the surface temperatures at 1100 UTC in degrees Kelvin. The large-scale northwest flow produced SIBL structure with the associated surface ducts along the line A to B. The striking land-sea temperature differences near shore produced localized sea breeze circulations with similar but more complex ducting conditions. Also notice that the radars are modeled near a gradient in the sea surface temperatures that also tend to decrease the height of the SIBL and advection ducts in the downwind direction.

Figure 2 is a plot of potential temperature every 100 km from A to B. Potential temperature is a conserved thermodynamic variable in a well-mixed marine atmospheric boundary layer (MABL). The positive slope indicates thermal stability that dampens turbulent mixing, subtracts from the 0.128 in (1) and nudges *dM/dz* toward super refraction.

Figure 3 is a plot of water vapor mixing ratio for every 100 km from A to B. Water vapor mixing ratio is also a conserved thermodynamic variable in a well-mixed MABL. The negative slope further subtracts from the 0.128 in (1). It is rare that thermal stability or a positive slope in potential temperature alone can produce ducting. It usually requires decreasing water vapor with height to drive the left side of (1) less than zero.

The gradient structure in Figs 2 and 3 is strong enough to force *dM/dz* negative as shown by the strong ducting profiles in Fig. 4. Notice how the ducting structure persists for 500 km. The duct height increases in the downwind direction out to 400 km. Between 400 and 500 km, the SIBL or duct height decreases in response to a cooler sea surface.

Figure 5 represents the modeled detection areas by the notional S-band radar of a notional target at 10 m ASL. Radar detection was modeled from 0 to 150 km. The white areas on the left indicate detection in a standard atmosphere and the white areas on the right indicate detection at 1100 UTC on May 14, 2009 using the refractivity field resolved by COAMPS®. The yellow range rings occur for every 30 km. It is obvious that RF energy has been trapped near the surface in the modeled refractivity field.

Figure 6 represents the modeled detection areas by the notional C-band radar of the same notional target at 10 m ASL for a standard atmosphere on the left and the modeled atmosphere on the right. The pattern is similar to S-band but the skip zones are narrower.

Figure 7 depicts the modeled detection areas by the notional X-band radar of the same notional target at 10 m ASL for a standard atmosphere on the left and the modeled atmosphere on the right. It can be seen that the skip zones are narrower than those at C-band.

It can be seen in Figs 5–7 that significant enhanced radar detection relative to a standard atmosphere is modeled for S-, C-, and X-band, respectively. The major difference is that the skip zone dimensions decrease with decreasing wavelength.

Figure 8 contains similar plots for the notional S-band radar where the same notional target, now at 100 m ASL, is being detected by the same notional S-band radar. Notice that for most of the azimuth angles, the detection range is below that for a standard atmosphere. At 40° azimuth from the radar, the close in detection range is reduced from 50 to 30 km with other detection areas near 60 and 75 km. A similar reduction in close-in detection range is observed at 220° azimuth but without the discontinuous detection areas

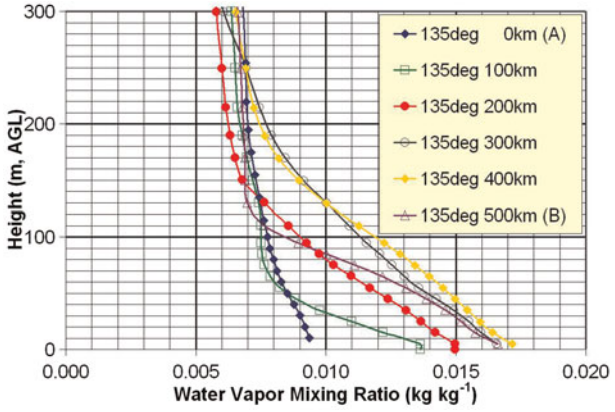

Fig. 3. Water vapor mixing ratio every 100 km from A to B as modeled by COAMPS® for 1100 UTC on May 14, 2009. The thermal stability prevents turbulent vertical mixing of water vapor from the surface.

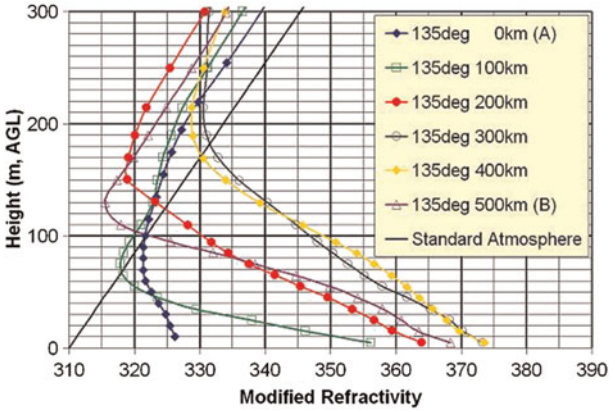

Fig. 4. Modified refractivity every 100 km from A to B as modeled by COAMPS® for 1100 UTC on May 14, 2009. Strong surface ducts are modeled downrange to 500 km.

https://doi.org/10.1017/S1759078711000225 Published online by Cambridge University Press

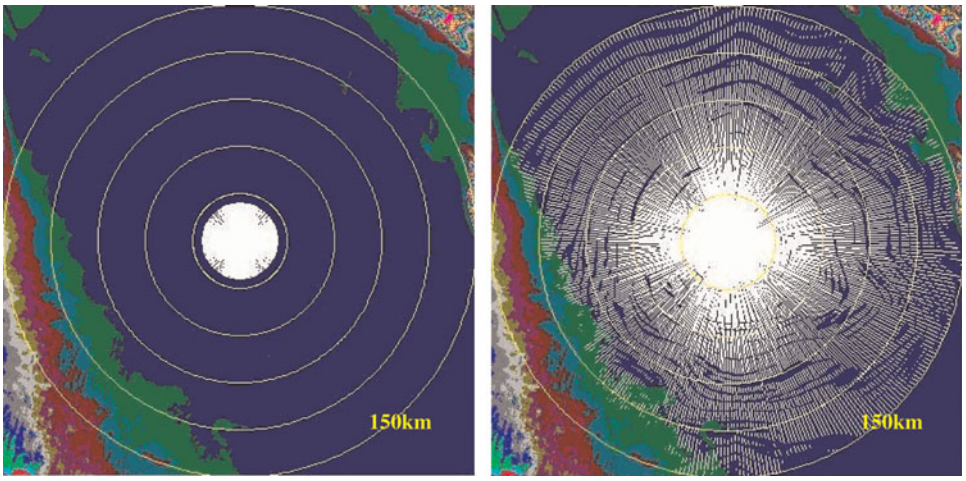

Fig. 5. Notional S-band radar detection areas in white of a notional target at 10 m ASL. The image on the left is an AREPS model in a standard atmosphere. The image on the right is a COAMPS®/AREPS model for 1100 UTC on May 14, 2009.

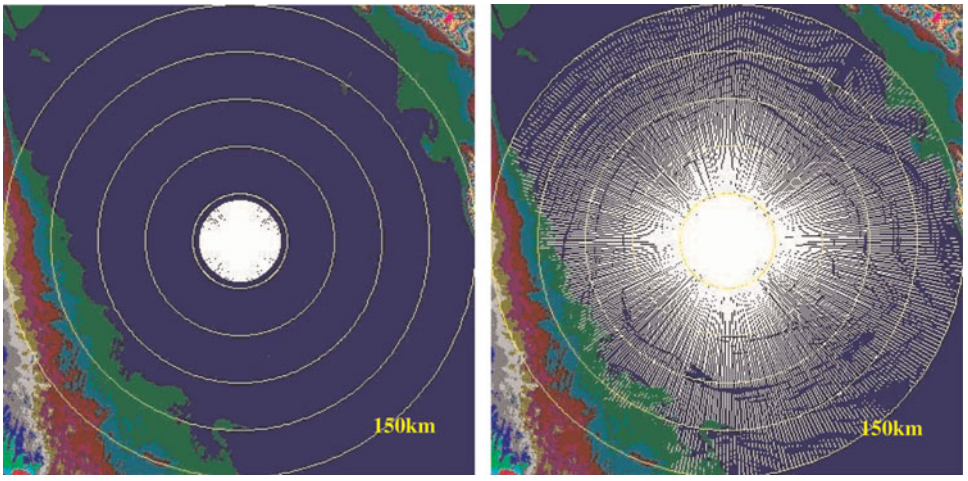

Fig. 6. Notional C-band radar detection areas in white of a notional target at 10 m ASL. The image on the left is an AREPS model in a standard atmosphere. The image on the right is a COAMPS®/AREPS model for 1100 UTC on May 14, 2009.

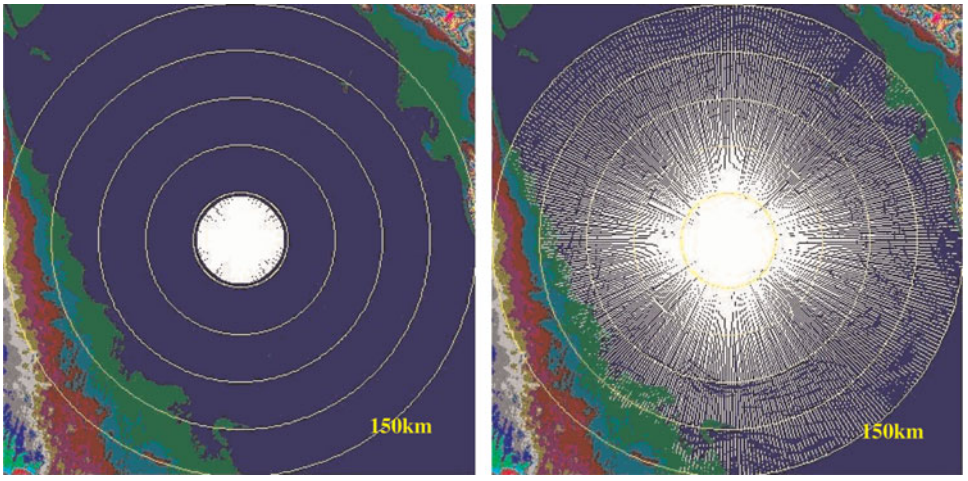

Fig. 7. Notional X-band radar detection areas in white of a notional target at 10 m ASL. The image on the left is an AREPS model in a standard atmosphere. The image on the right is a COAMPS®/AREPS model for 1100 UTC on May 14, 2009.

https://doi.org/10.1017/S1759078711000225 Published online by Cambridge University Press

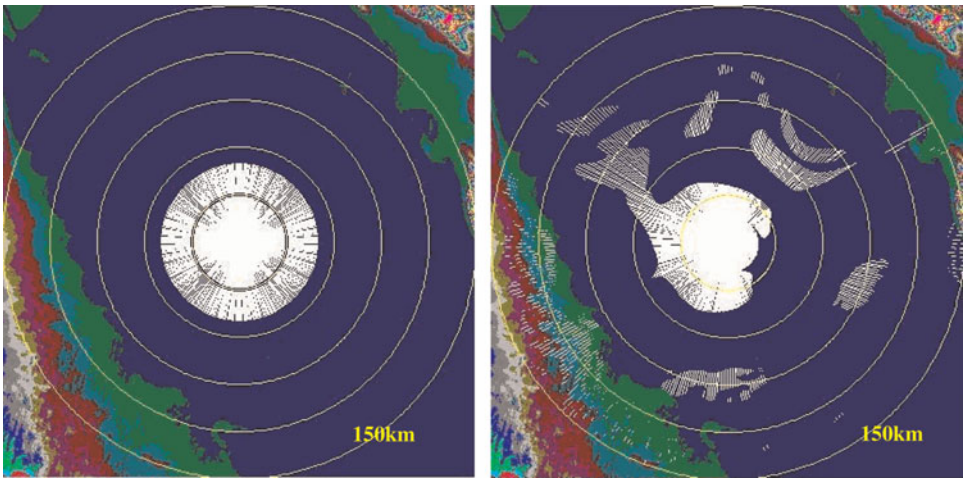

Fig. 8. Notional S-band radar detection areas in white of a notional target at 100 m ASL. The image on the left is an AREPS model in a standard atmosphere. The image on the right is a COAMPS®/AREPS model for 1100 UTC on May 14, 2009.

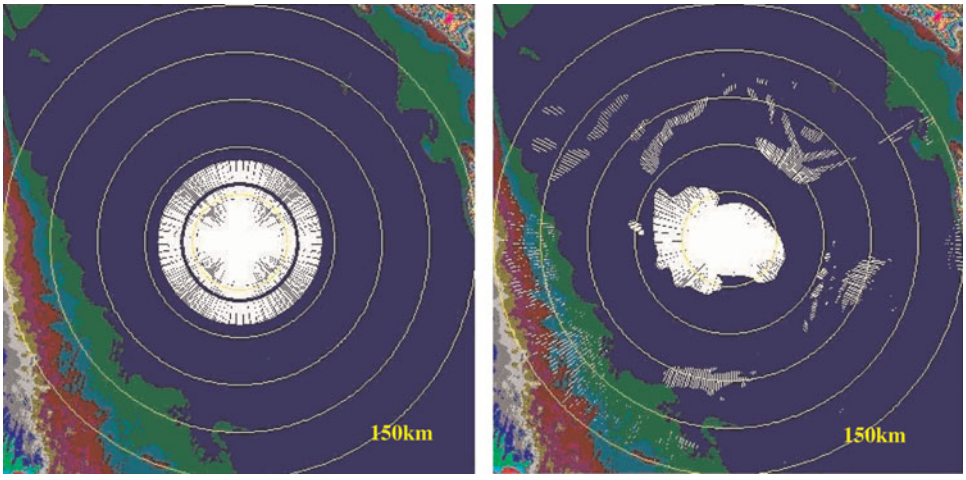

Fig. 9. Notional C-band radar detection areas in white of a notional target at 100 m ASL. The image on the left is an AREPS model in a standard atmosphere. The image on the right is a COAMPS®/AREPS model for 1100 UTC on May 14, 2009.

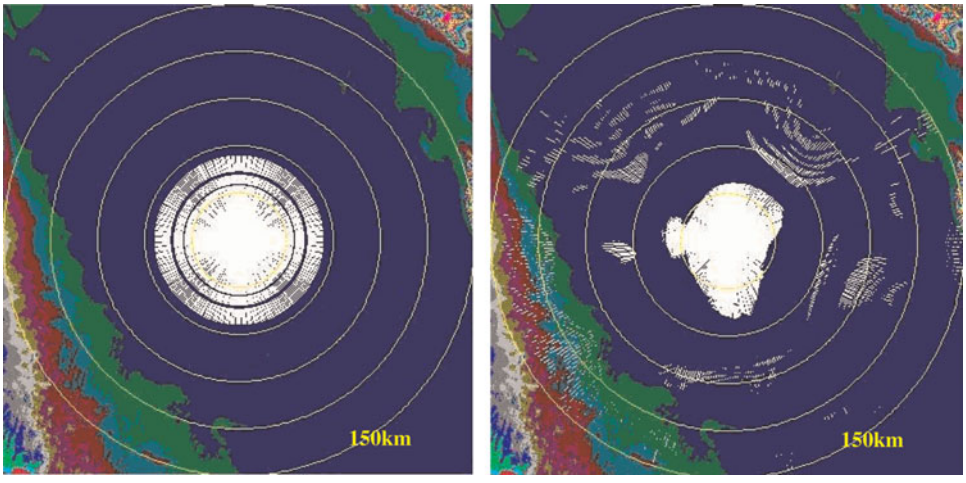

Fig. 10. Notional X-band radar detection areas in white of a notional target at 100 m ASL. The image on the left is an AREPS model in a standard atmosphere. The image on the right is a COAMPS®/AREPS model for 1100 UTC on May 14, 2009.

https://doi.org/10.1017/S1759078711000225 Published online by Cambridge University Press

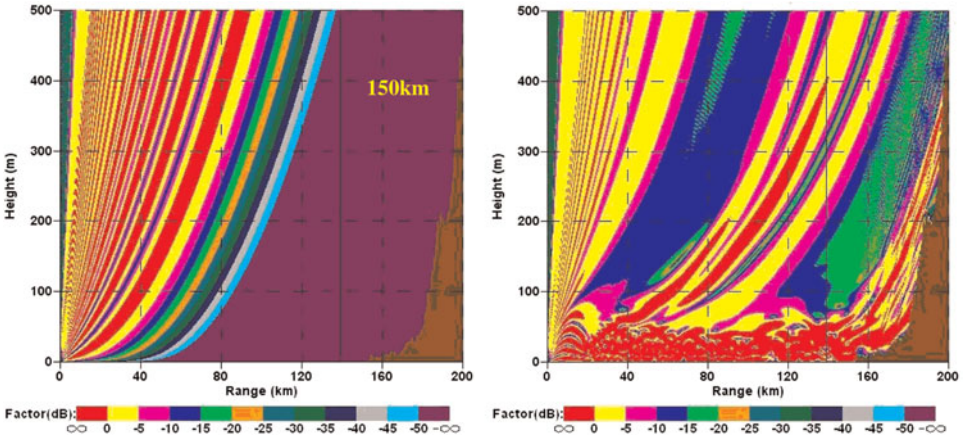

Fig. 11. One-way propagation factor from 0 to 200 km from the notional S-band radar along the 40° azimuth. Height is indicated from 0 to 500 m ASL. The figure on the left is for a standard atmosphere and the figure on the right is for the COAMPS® refractivity field. Values of propagation factor greater than zero are indicated by red.

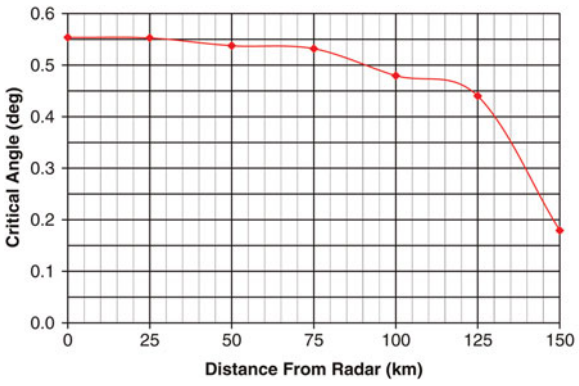

Fig. 12. Critical elevation angle for energy escape from the duct along the 40° azimuth.

downrange. Detection over land, not expected in a standard atmosphere, is observed to the east, southwest, and west.

Figure 9 contains similar plots for the notional C-band radar with the same notional target, now at 100 m ASL. Notice the detection pattern is somewhat different than that at S-band. Close-in detection is generally reduced relative to a standard atmosphere and the enhanced detection along 310° at S-band is absent at C-band. Notional target detection over land is observed to the east, southwest, and west similarly to S-band.

Figure 10 contains similar plots for the notional X-band radar where the same notional target is now at 100 m ASL is being detected by the notional X-band radar. Notice that for all of the azimuth angles, the detection range is below that for a standard atmosphere. The pattern of discontinuous target detection similar to that at S- and C-band is still observed. Over land detection is also modeled at X-band.

IV. PROPAGATION FIELDS

Two-way propagation factor is shown as F^4 in the radar equation given in equation (2). Depending on the nature of the propagation regime, propagation factor can be plus or minus 30 dB:

$$\frac{P_r}{P_t} = \frac{G^2 \lambda^2 \sigma}{(4\pi)^3 R^4} F^4 . \qquad (2)$$

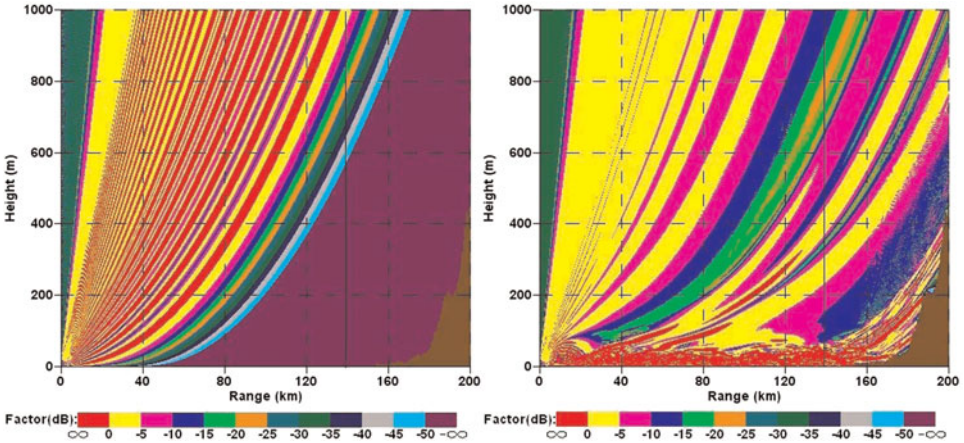

Fig. 13. One-way propagation factor from 0 to 200 km from the notional C-band radar along the 40° azimuth. Height is indicated from 0 to 1000 m ASL. The figure on the left is for a standard atmosphere and the figure on the right is for the COAMPS® refractivity field. Values of propagation factor greater than zero are indicated by red.

https://doi.org/10.1017/S1759078711000225 Published online by Cambridge University Press

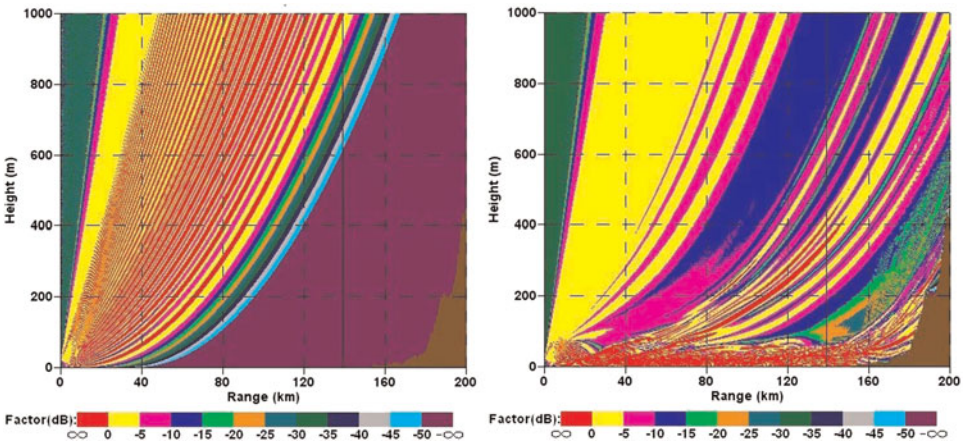

Fig. 14. One-way propagation factor from 0 to 200 km from the notional X-band radar along the 40° azimuth. Height is indicated from 0 to 1000 m ASL. The figure on the left is for a standard atmosphere and the figure on the right is for the COAMPS® refractivity field. Values of propagation factor greater than zero are indicated by red.

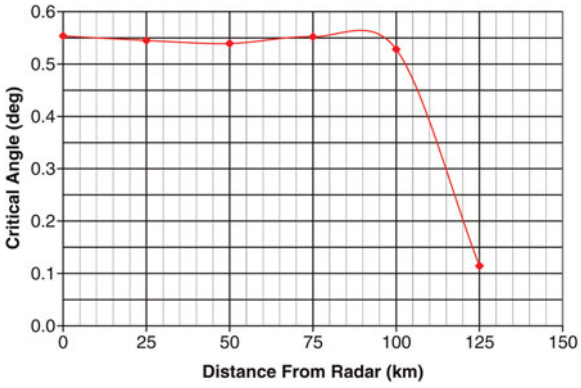

Fig. 15. Critical elevation angle for energy escape from the duct along the 220° azimuth.

A) Forty degrees azimuth

Figure 11 is a plot of one-way propagation factor for the notional S-band radar located at the star in Fig. 1 and pointed along the 40° azimuth. The plot on the left is for a standard atmosphere and the plot on the right is for the COAMPS® modeled refractivity field.

Near the surface, at 10 m ASL, it is clear that the energy is trapped in a shallow layer near 50 m ASL all the way to and across land indicated by brown. At 100 m ASL, energy is observed escaping from the duct near 60 and 75 km downrange. This is due to a reduction in elevation critical angle for energy escape from the duct that is proportional to the square root of twice the difference in the change in modified refractivity across the duct as shown in [7]

$$\alpha_c = 0.0573(2\Delta M)^{0.5}. \quad (3)$$

This escape of energy allows for detection range near 60 and 75 km as indicated in Fig. 11. The critical angle for the 40° azimuth is plotted in Fig. 12. The wavelength-independent critical angle significantly decreases beginning 25 km downrange from the radar. This indicates that the duct strength decreases toward land. At this point, energy begins to escape the duct and is refracted upwards downrange such that positive propagation factor is available at 100 m ASL in Fig. 11. Closer in, the loss of propagation factor compared to a standard atmosphere between 40 and 50 km accounts for the loss of detection at these ranges for the notional target at 100 m ASL.

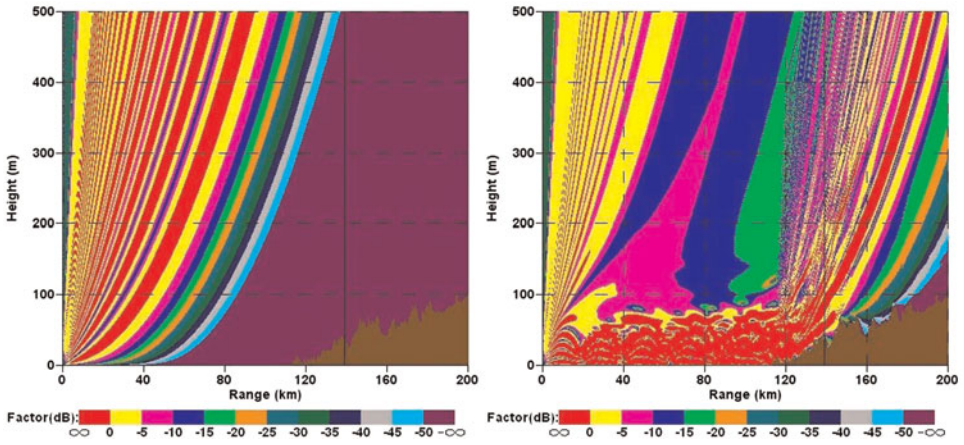

Fig. 16. One-way propagation factor from 0 to 200 km from the notional S-band radar along the 220° azimuth. Height is indicated from 0 to 500 m ASL. The figure on the left is for a standard atmosphere and the figure on the right is for the COAMPS® refractivity field. Values of propagation factor greater than zero are indicated by red.

https://doi.org/10.1017/S1759078711000225 Published online by Cambridge University Press

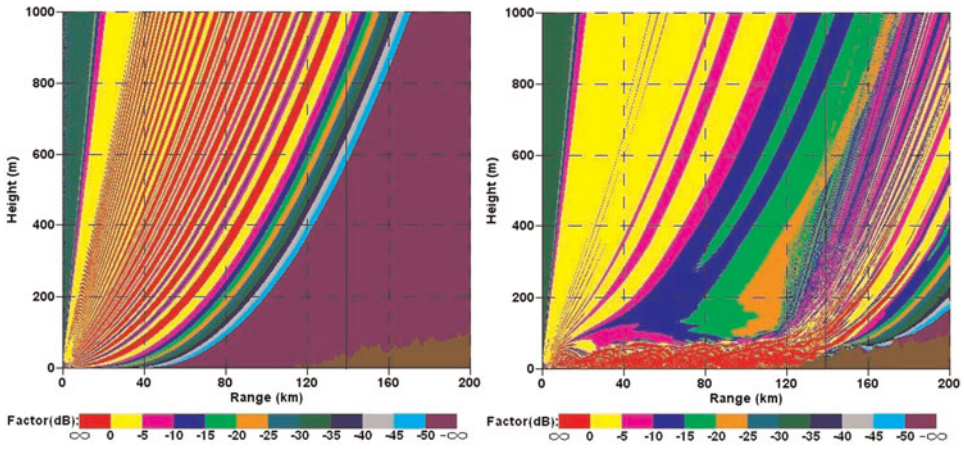

Fig. 17. One-way propagation factor from 0 to 200 km from the notional C-band radar along the 220° azimuth. Height is indicated from 0 to 1000 m ASL. The figure on the left is for a standard atmosphere and the figure on the right is for the COAMPS® refractivity field. Values of propagation factor greater than zero are indicated by red.

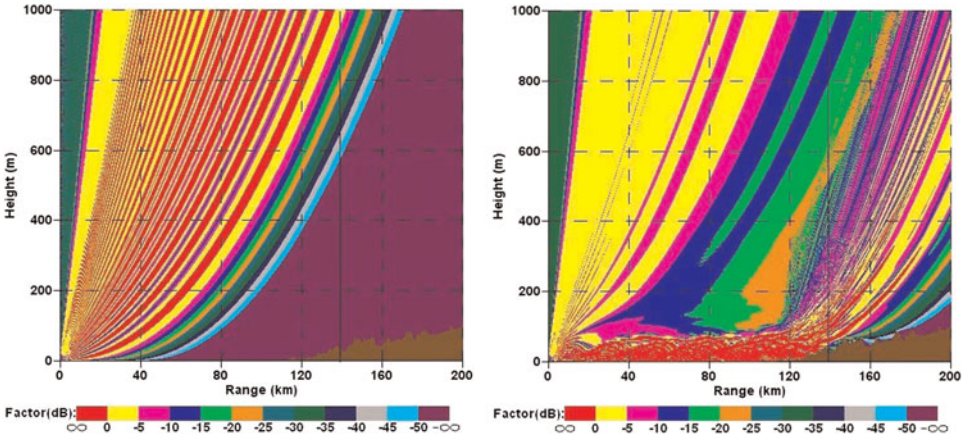

Fig. 18. One-way propagation factor from 0 to 200 km from the notional X-band radar along the 220° azimuth. Height is indicated from 0 to 1000 m ASL. The figure on the left is for a standard atmosphere and the figure on the right is for the COAMPS® refractivity field. Values of propagation factor greater than zero are indicated by red.

One-way propagation factor for the notional C-band radar along the 40° azimuth is displayed in Fig. 13. Notice that the standard atmosphere lobes and escaping energy lobes are narrower than at S-band.

One-way propagation factor for the notional X-band radar along the 40° azimuth is displayed in Fig. 14. Again it is demonstrated that the standard atmosphere lobes and the escaping energy lobes narrow with increasing frequency. This is the source of the narrowing target detection bands in Figs 11–13, respectively.

B) Two hundred and twenty degrees azimuth

Figure 15 represents the critical elevation angle along the 220° azimuth. The critical angle and thus the duct strength remains fairly constant out 100 km from the radar. Then the critical angle rapidly decreases allowing energy to escape the duct.

Figure 16 represents standard and modeled propagation factor along the 220° azimuth for the notional S-band radar. At this bearing, notional target detection at 100 m ASL is 5 km below that in a standard atmosphere. There are also no discontinuous target detection areas downrange as there were at 40° azimuth. But near land as the critical angle rapidly decreases, RF energy escapes the duct and target detection is indicated over land.

A similar graphic of standard and modeled propagation factor along the 220° azimuth for the notional C-band radar is displayed in Fig. 17. At this bearing, notional target detection range at 100 m ASL is 9 km below that in a standard atmosphere. There are also no discontinuous target detection areas downrange as there were at 40° azimuth. But near land as the critical angle rapidly decreases, RF energy escapes the duct and target detection is indicated over land. This is similar to target detection behavior at S-band but once again, the escaping energy is in narrower lobes than at S-band.

One-way propagation factor for the notional X-band radar along the 220° azimuth is displayed in Fig. 18. The pattern is similar to that at S- and C-band due to the wavelength-independent critical angle profile.

V. CONCLUSIONS

Warm dry air flowing over colder sea surfaces can produce surface RF ducting that extends for hundred of kilometers. Mesoscale NWP models coupled to modern parabolic

https://doi.org/10.1017/S1759078711000225 Published online by Cambridge University Press

equation RF propagation models provide a once unheard of view of the spatio-temporal intricacies of radar performance in these non-standard refractivity environments. Within the duct, radar detection of notional targets can extend for hundreds of kilometers. Above the duct, radar detection is determined by the critical elevation angle and the difference in modified refractivity across the duct. The dimensions of the above duct down range detection areas decrease with decreasing wavelength.

REFERENCES

[1] Smedman, A.; Bergstrom, H.; Grisogono, B.: Evolution of stable internal boundary layers over a cold sea. J. Geophys. Res., **102** (1997), 1091–1099.

[2] Marshall, R.E.; Horgan, K.L.: The Contribution of Dry Surface Air Over Land to the Strength of Radio Frequency Trapping Layers in the Sea Breeze Circulation, American Meteorological Society, J 8.2, San Diego, CA, January 2009.

[3] Marshall, R.E.; Haack, T.: Engineering demands placed on littoral radar due to non-standard propagation revealed by mesoscale numerical weather prediction technology, in *IEEE Radar Conf.*, Rome, Italy, May 2008.

[4] Haack, T.; Wang, C.; Garrett, S.; Glazer, A.; Mailhot, J.; Marshall, R.: A mesoscale model intercomparison of boundary layer refractivity and atmospheric ducting. J. Appl. Meteorol. Climatol., 49(12) 2010, 2437–2457.

[5] Patterson, W.L.: Advanced Refractive Effects Prediction System Version 3.0 Users Manual, Space and Naval Warfare Systems Center, San Diego, CA, 2006.

[6] Hodur, R. et al. The Coupled Ocean/Atmosphere Prediction System (COAMPS®). Oceanography, 15 (2002), 88–99.

[7] Dougherty, H.; Dutton, E.: The Role of Elevated Ducting for Radio Service and Interference Fields, NTIA Report-81-69, US Department of Commerce, March, 1981.

Robert E. Marshall received a B.Sci. and M.Sci. in electrical engineering from Virginia Tech in 1971 and 1973, respectively. He earned a Ph.D. in atmospheric science from North Carolina State University in 1995. Dr. Marshall is a senior scientist at the Naval Surface Warfare Center in Dahlgren, Virginia where he performs research in RF propagation and meteorology.

Katherine L. Horgan received a B.S. in meteorology from North Carolina State University in 2006. She is currently working on her M.S. in atmospheric science from Texas Tech University. Katherine is a scientist at the Naval Surface Warfare Center in Dahlgren, Virginia, where she performs research in meteorology and RF propagation.

https://doi.org/10.1017/S1759078711000225 Published online by Cambridge University Press